Applied Catalysis B: Environmental 342 (2024) 123418

Contents lists available at ScienceDirect

Applied Catalysis B: Environmental

journal homepage: www.elsevier.com/locate/apcatb

Metal-porphyrin-based three-dimensional covalent organic frameworks for electrocatalytic nitrogen reduction

Zhen Shan [a,1], Yuntong Sun [a,1], Miaomiao Wu [a], Yingtang Zhou [c], Jinjian Wang [a], Sheng Chen [a,*], Rui Wang [a,*], Gen Zhang [a,b,**]

[a] Key Laboratory for Soft Chemistry and Functional Materials of Ministry of Education, School of Chemistry and Chemical Engineering, Nanjing University of Science and Technology, Nanjing, Jiangsu 210094, China

[b] Key Laboratory of Preclinical Study for New Drugs of Gansu Province, School of Basic Medical Sciences & Research Unit of Peptide Science, Chinese Academy of Medical Sciences, 2019RU066, Lanzhou University, Lanzhou 730000, China

[c] National Engineering Research Center for Marine Aquaculture, Marine Science and Technology College, Zhejiang Ocean University, Zhoushan 316004, China

ARTICLE INFO

Keywords:
3D covalent organic frameworks
scu/flu topology
Electrocatalytic
Nitrogen reduction reaction

ABSTRACT

Electrocatalytic nitrogen reduction reaction (NRR) under ambient conditions presents a sustainable method for renewable ammonia production. However, the development of high-performance NRR electrocatalysts with satisfactory efficiency and selectivity remains a significant challenge. Herein, we design and synthesize two metal-porphyrin based 3D COFs bearing metal-N_4 catalytic sites with different 3D spatial arrangements (*scu* and *flu* topologies) for this purpose. The anchoring of metal ions (Fe, Cu) at the center of the planar conjugated-porphyrin ring enhances the activity and selectivity of electrocatalytic NRR. Significantly, the 3D COFs with Fe-N_4 catalytic sites feature higher NH_3 yield and Faradaic efficiency (94.26 ± 4.9 μg h^{-1} mg^{-1} and 18.37 ± 0.96 % at −0.5 V *vs* RHE, reversible hydrogen electrode) than those with Cu-N_4 centers, making them promising candidates for NRR electrocatalysts. This work not only enriches the topological library of 3D COFs, but also provides an idea for the rational design of metal porphyrin-based COFs for NH_3 production.

1. Introduction

Ammonia (NH_3) is one of the most produced chemicals in chemical industry due to its high energy density and large hydrogen content. As an important energy carrier, NH_3 is used in large quantities in the production of many compounds, such as fertilizers, dyes, pigments, drugs, explosives, resins, and light-emitting diodes [1,2]. In order to meet the increasing demand for NH_3, it is very urgent to develop ultra-efficient NH_3 production routes under mild conditions to replace the traditional Harber-Bosch process required high temperature, high pressure and high energy consumption [3,4]. In recent years, electrocatalysis technology has played a key role in the field of NRR and has made remarkable progress [5–8]. However, the high kinetic and thermodynamic stability of N≡N triple bond makes it difficult to activate N_2 under ambient conditions. In addition, the competitive two-electron ($2e^-$) hydrogen evolution reaction (HER) with a lower energy barrier in similar potential ranges greatly reduces the yield of NRR. How to design efficient electrocatalysts to improve NRR efficiency and inhibit HER process is a great challenge. Metal-heteroatom-doped carbon-rich materials have been widely concerned by researchers because of their adjustable catalytic environment [9–13], determination of active sites and maximum atomic utilization, but their poor stability and recyclability hinder their practical applications. Therefore, it is of great significance to design and develop NRR electrocatalysts with high stability and high activity.

Covalent organic frameworks (COFs), as an emerging class of crystalline porous polymers, have unique porosity, abundant reachability of active sites, chemical stability and pre-designed topology [14–16]. The extended structure of periodic skeleton and ordered pores of COFs provides abundant docking sites for catalytic active species, and offers a large specific surface area for reactant adsorption and product desorption [17,18]. In recent years, porphyrin (Por-) based COFs with unique

* Corresponding authors.
** Corresponding author at: Key Laboratory for Soft Chemistry and Functional Materials of Ministry of Education, School of Chemistry and Chemical Engineering, Nanjing University of Science and Technology, Nanjing, Jiangsu 210094, China.
E-mail addresses: sheng.chen@njust.edu.cn (S. Chen), wangrui@lzu.edu.cn (R. Wang), zhanggen@njust.edu.cn (G. Zhang).
[1] Zhen Shan and Yuntong Sun contributed equally to this work.

https://doi.org/10.1016/j.apcatb.2023.123418
Received 13 June 2023; Received in revised form 9 October 2023; Accepted 19 October 2023
Available online 21 October 2023
0926-3373/© 2023 Elsevier B.V. All rights reserved.

structural characteristics and excellent optical and electrical properties have attracted extensive attention of researchers [19,20]. Owing to the planar N_4 coordination and large π-conjugated systems of porphyrins, they allow different types of metal ions to anchor into their cores and improve the affinity for inert molecules and reduce the activation energy, thus making great progress in electrocatalytic water decomposition [21–23], oxygen reduction [24–27] and carbon dioxide reduction [28,29]. To date, most of Por-COFs used for catalysis are 2D structure [30,31], while the metal-N_4 catalytic sites are mainly buried in 2D layered structures, resulting in insufficient exposure to substrates that limits the catalytic efficiency. In contrast, 3D network COFs with interconnected pore structures and higher surface areas that could expose more active sites, and are theoretically more favorable for electrocatalysis [32], but less progress been exploited in this area due to the limitation of building blocks and severe crystallization problems. How to arrange metal-N_4 units in 3D space with unique topologies through reticular chemistry, and systematically investigates the influence of topologies and metals on NRR remains elusive.

Up to date, only a dozen of 3D COF topologies have been reported, most of which are based on 3–, 4– or 6-connected knots. For instance, the 3D COF with a twofold interpenetrating ***acs*** network connected by 6 organic cages [33] and 3D COFs with ***stp***, [34,35] ***ceq***, [36] and ***hea*** [37, 38] topologies based on triterpene-based building blocks have been developed. Since Yaghi and co-authors disclosed an *in situ* self-coagulation strategy to prepare 8-connected COFs with reticular ***bcu*** net, [39] the design of highly connected linkers (≥ 8) has received extensive attention (Scheme 1). Carbon backbones containing high-valence stereoscopic molecular nodes will greatly expand the 3D COF structure and lead to the explosion of new 3D COF topologies [40–42]. Though most of the newly developed 3D COFs are used in gas adsorption and separation [43–45], the researches on their catalytic applications remains unexploited. Hence, the design and synthesis of 3D COFs with new topological structure based on functionalized porphyrin mods is of great significance in the field of electrocatalytic NRR.

2. Experimental section

2.1. Materials and general methods

Mesitylene, dioxane and (4-formylphenyl)boronic acid, $Pd(PPh_3)_4$, anhydrous K_2CO_3 were purchased from Energy Chemical (Shanghai, China). *N*,*N*-dimethylformamide, tetrahydrofuran (THF) were purchased from *J&K* Chemicals (Shanghai, China). All the commercial chemicals were directly used without further purification.

2.2. Synthesis of COFs

Synthesis of NUST-18: TTEP (36.2 mg, 0.025 mmol) and 1,2,4,5-tetrakis-(4-aminophenyl) benzene (TAPB) (22.1 mg, 0.05 mmol) were weighed into a glass ampoule with mesitylene (2.0 mL) and dioxane (2.0 mL). The solution was ultrasound for 5 min, and then 6 M acetic acid (0.3 mL) was added into the glass ampoule as catalyst. The glass ampoule was flash frozen at 77 K using the liquid nitrogen bath and degassed by freeze-pump-thaw three times, and then was flame sealed. The glass ampoule was placed at 120 °C for 3 days. The dark brown solid was isolated by centrifugation and washed with MeOH (3 ×10 mL) and further purified by Soxhlet extraction with THF and $CHCl_3$. The sample was then transferred to vacuum chamber and evacuated to 20 mTorr at 50 °C for 24 h, yielding NUST-18 as brown powders (Yield: 45.2 mg, 82.6 %).

Synthesis of NUST-19: TTEP (36.2 mg, 0.025 mmol) and tetrahedral diamine tetrakis(4-aminophenyl)methane (TAPM) (19.0 mg, 0.05 mmol) were weighed into a glass ampoule with mesitylene (2.0 mL) and dioxane (2.0 mL). The solution was ultrasound for 5 min, and then 6 M acetic acid (0.3 mL) was added into the glass ampoule as catalyst. The glass ampoule was flash frozen at 77 K using the liquid nitrogen bath and degassed by freeze-pump-thaw three times, and then was flame sealed. The glass ampoule was placed at 120 °C for 3 days. The dark brown solid was isolated by centrifugation and washed with MeOH and further purified by Soxhlet extraction with THF and $CHCl_3$. The sample was then transferred to vacuum chamber and evacuated to 20 mTorr at 50 °C for 24 h, yielding NUST-19 as brown powders (Yield: 39.5 mg, 76.5 %).

2.3. Electrode preparation and Cathodic NRR test

5 mg of as-formed catalysts, 1 mg of acetylene black (conductive agent), and 30 μL of Nafion solution (5 wt%) were dispersed in 1 mL of isopropanol/DI-water (v/v = 4:1) mixed solutions, which were ultrasonicated for 30 min (mins) to form a uniform catalyst ink. Next, 120 μL

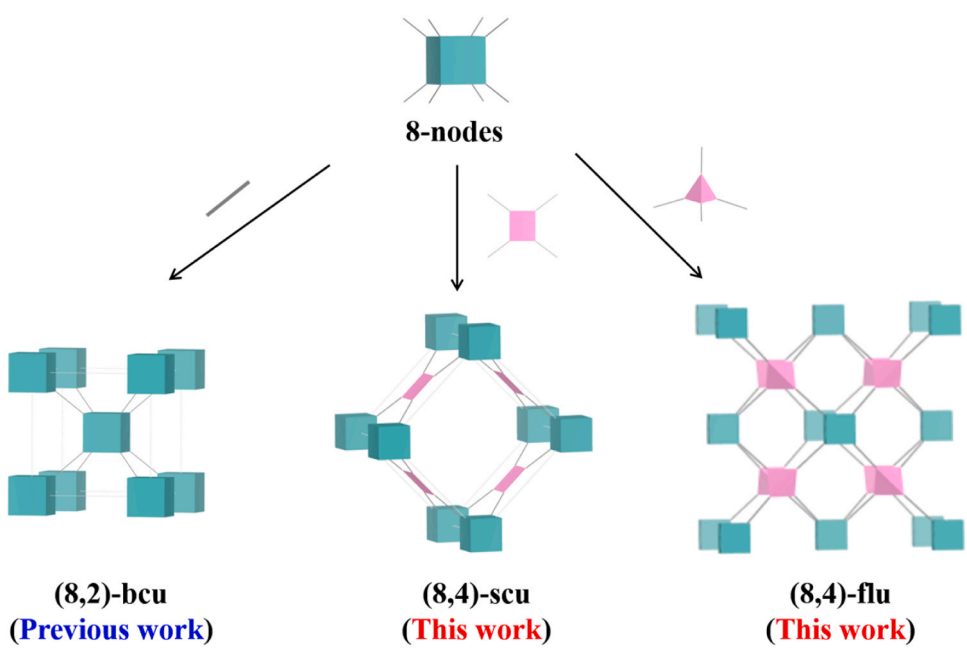

Scheme 1. Topologies based on 8-linked cubic nodes.

of the above catalyst ink was transferred to a 1.0 × 3.0 cm^2 gas diffusion layer (GDL), where the effective catalytic area is 1 cm^2 and mass loading is 0.2 mg cm^{-2}.

Cathodic nitrogen reduction reaction (NRR) were studied in a three-electrode flow-type electrolytic cell under Ar- or N_2-saturated conditions connected to a CHI 760E electrochemical workstation using the as-formed catalysts as working electrode, GDL as counter electrode, Ag/AgCl/KCl (saturated) as reference electrode, 0.1 M Na_2SO_4 aqueous solution as electrolyte, Nafion 115 membrane as the separator and 0.05 M H_2SO_4 aqueous solution as exhaust gas absorption chamber. The feeding rates of electrolyte and gas flow (N_2 or Ar) were 40 and 20 mL min^{-1}, respectively.

Note that Nafion may become the ammonia contamination because it can absorb and release ammonia. Therefore, Nafion membrane was pretreated before being used. It was sequentially pretreated in H_2O_2 aqueous solution (5 wt%, 80 °C) for 3 hrs, DI-water (80 °C) for 1 hr, 0.5 M H_2SO_4 solution (80 °C) for 2 hrs, 0.5 M H_2SO_4 solution (100 °C) for 8 h, DI-water (80 °C) for 1 h and rinsed in DI-water several times.

Before electrochemical test, the electrolyte was purged with Ar or N_2 flow (pretreated by 0.5 M H_2SO_4 and 1 M KOH aqueous solution) for 30 min. During electrolysis, catholyte and anolyte are pumped through corresponding chambers separated by Nafion 115 membrane and pumped out separate reservoirs. The product is extracted and collected by acid absorption chambers isolated from external pollution, ensuring the accuracy of the experiment. To analyze NRR activities, linear sweep voltammograms (LSVs) was performed at a scan rate of 5 mV s^{-1} in the potential range of − 0.8 to 0.6 V (*vs.* RHE), and chronoamperometric test was carried out at different potentials for 1 hr with continuous saturation Ar or N_2 flow in the electrochemical system. In order to avoid external pollutions, the electrolytes were prepared and used fresh, and the first cycle data is discarded.

The long-term stability was examined by chronoamperometric response at − 0.5 V (*vs.* RHE) up to 10 h. The corresponding LSVs before and after stability testing were collected for comparison purpose. The electrochemical specific surface area (ECSA) of Fe@NUST-18 and other comparison samples were obtained by CVs methods [2]. The data was collected at different scan rates from 80 to 160 mV s^{-1}. The plots of current difference ($\Delta J = J_a - J_c$) against scan rates were nearly linear and the double layer capacitance (C_{dl}, mF) was obtained.

The electrochemical active surface area (*ECSA*) value of Fe@NUST-18, Cu@NUST-18 and NUST-18 can be evaluated by the following formula:

$$ECSA = C_{dl} / C_s \text{ per cm}^{-2}$$

Where $C_s = 0.035$ mF cm^{-2} (typical reported value).

The TOFs of NH_3 production in NRR was calculated.

$$TOF_{NH3} = n_{(NH3)} / (t * n_{site})$$

where $n_{(NH3)}$ (moL) is the moles of produced NH_3, t (h) is the reduction reaction time,

n site (moL) is the moles of Fe or Cu in the catalysts.

2.4. $^{15}N_2$ isotope labeling experiment

Isotopic labelling experiment with $^{15}N_2$ feeding gas was used for clarifying the source of NH_3 during NRR. Before the experiment, Ar gas was continuously passed through NRR electrolytic cell for 30 min. Next, NRR test was carried out for 4 hrs in a closed circulation electrochemical system saturated with ^{15}N gas at the flow rate of 20 mL min^{-1}. Finally, the electrolyte with product was collected, adjusted to pH= 2, and concentrated for ^1H NMR (nuclear magnetic resonance, 500 MHz) analyses.

3. Results and discussion

Herein, we design and synthesis of an 8-connected cubic porphyrin node to build up 3D COFs with unprecedented ***scu*** and ***flu*** topologies *via* [8 + 4] imine condensation with quadrilateral and tetrahedral anime monomers for electrocatalytic NRR. Two 3D Por-COFs with microporous channels were constructed *via* Schiff-base reaction between an 8-connected building block, 5,10,15,20-tetrayl(tetrakis(([1,1':3',1''-terphenyl]−4,4''-dicarbaldehyde)))-porphyrin (TTEP) and quadrilateral 1,2,4,5-tetrakis-(4-aminophenyl) benzene (TAPB) or tetrahedral tetrakis(4-aminophenyl)methane (TAPM) in a mixture of mesitylene and dioxane, and 6 M acetic acid as the catalyst at 120 °C for 72 h, denoted as NUST-18/19 with ***scu/flu*** topology based on reticular chemistry, respectively (Scheme 1 and Fig. 1).

The complete imine condensation between monomers of NUST-18/19 were confirmed through various spectroscopy. The formation of imine bands was verified by Fourier transform infrared spectroscopy (FT-IR) with new stretching vibration bands at ~1603 cm^{-1} for NUST-18 (Fig. S3) and ~1606 cm^{-1} for NUST-19 (Fig. S4). Additionally, the near-disappearance of characteristic N-H (~3335 cm^{-1} for TAPB, ~3398 cm^{-1} for TAPM) and C═O (~1685 cm^{-1} for TTEP) stretching bands confirmed the complete condensation of aldehyde and amine groups. Solid-state ^{13}C NMR spectroscopy indicated the presence of carbons from imine groups by the peaks at 169/168 ppm for NUST-18/19 (Fig. S1, S2), which further confirmed the formation of imine bonds. Scanning electron microscopy (SEM) and transmission electron microscopy (TEM) demonstrated the flat stick shape morphology for NUST-18/19 (Fig. S10-S13). The thermal stability of COFs was characterized by thermogravimetric analysis (TGA) under nitrogen atmosphere. The decomposition temperature was up to ~ 410 °C for NUST-18 (Fig. S5), and ~ 420 °C for NUST-19 (Fig. S6).

3.1. Crystal Structure

The structure definition of NUST-18/19 were elucidated by PXRD analysis together with structural simulations. By carefully screening the potential nets based on cubic d4R SBUs (secondary building units) from Reticular Chemistry Structure Resource (RCSR), we found that only ***scu*** and ***csq*** topologies seem to conform to NUST-18, and ***flu*** topology conform to NUST-19. By building structural models, the experimental PXRD patterns of NUST-18 were in agreement with the simulated patterns obtained from model the ***scu*** topology (Fig. 2a). NUST-19 belongs to the ***flu*** topology, and the experimental PXRD patterns were in good agreement with the simulated values (Fig. 2d). By carrying out full profile pattern matching (Pawley) refinement, NUST-18 adopted space group *C2/M* (No.12) with unit cell parameters of a = 53.94 Å, b = 37.01 Å, c = 21.05 Å; $\alpha = 90°$, $\beta = 88.60°$, $\gamma = 90°$, and exhibited intensive main diffraction peaks at 2.89° (110), 4.12° (001), 5.06° (111), and 8.49° (131), respectively. NUST-19 adopted space group *FMMM* (No. 69) with unit cell parameters of a = 53.87 Å, b = 49.58 Å, c = 47.52 Å; $\alpha = \beta = \gamma = 90°$, and exhibited intensive main diffraction peaks at 3.01° (111) 3.68° (002), 5.00° (202), and 8.37° (422), respectively. The refinement results illustrated good agreement factors (R_{wp} = 2.54 % and R_p = 1.47 % for NUST-18; R_{wp} = 2.85 % and R_p = 1.66 % for NUST-19). We also consider ***ceq***-based structural model and simulate this topology, but the simulated patterns are inconsistent with the experimental PXRD patterns (Fig. S14, S15). We also simulated the 2-fold interpenetrating structure models and found that the same PXRD patterns were not generated as in the experiment (Fig. S16-S19). Considering these results, NUST-18/19 were proposed to have the expected 3D frameworks with the ***scu*** net and ***flu*** net, respectively. The crystallinity and nanoscale porosity of NUST-18/19 was also revealed by high-resolution transmission electron microscopy (HR-TEM), where crystallites with periodic channel-like features were observed (Fig. S12, S13).

The porosity and specific surface areas of the COFs were carried out

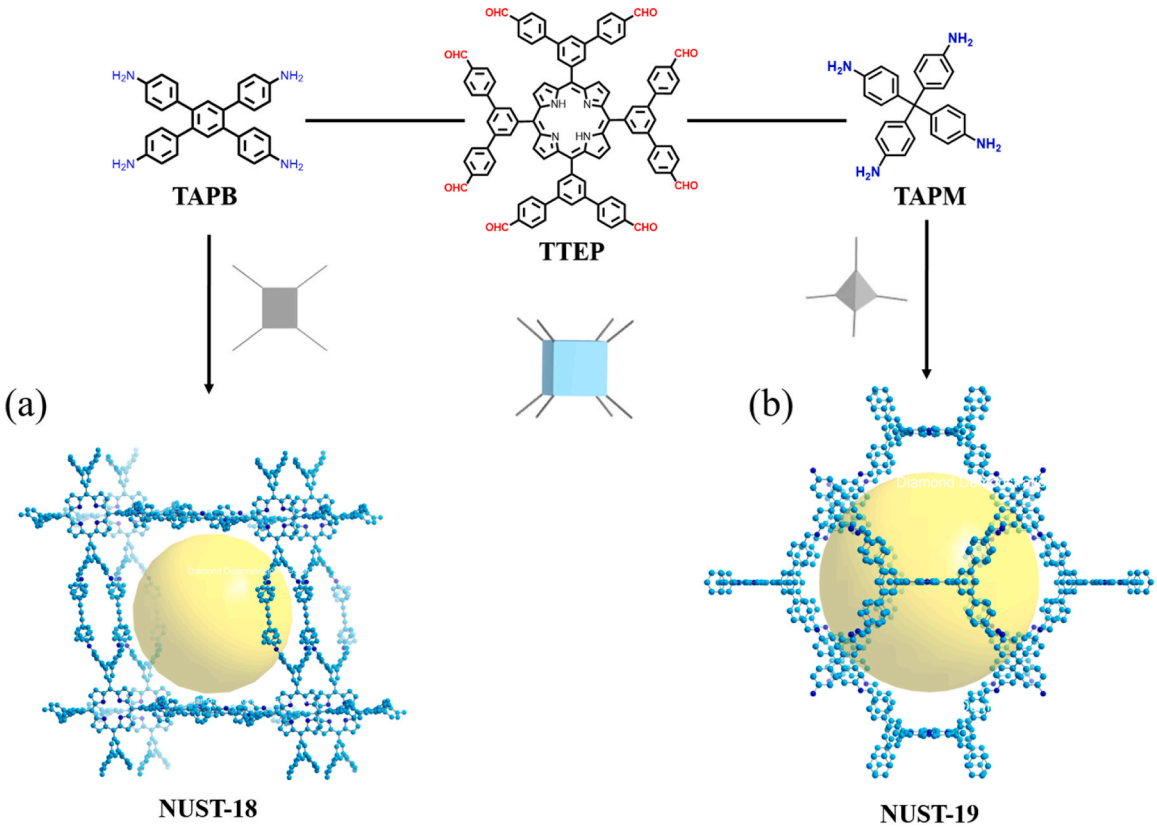

Fig. 1. Schematic synthetic process of COFs. (a) Structural characterization of NUST-18 with an expanded [8 + 4] connected network (***scu*** topology); (b) Structural characterization of NUST-19 with an expanded [8 + 4] connected network (***flu*** topology).

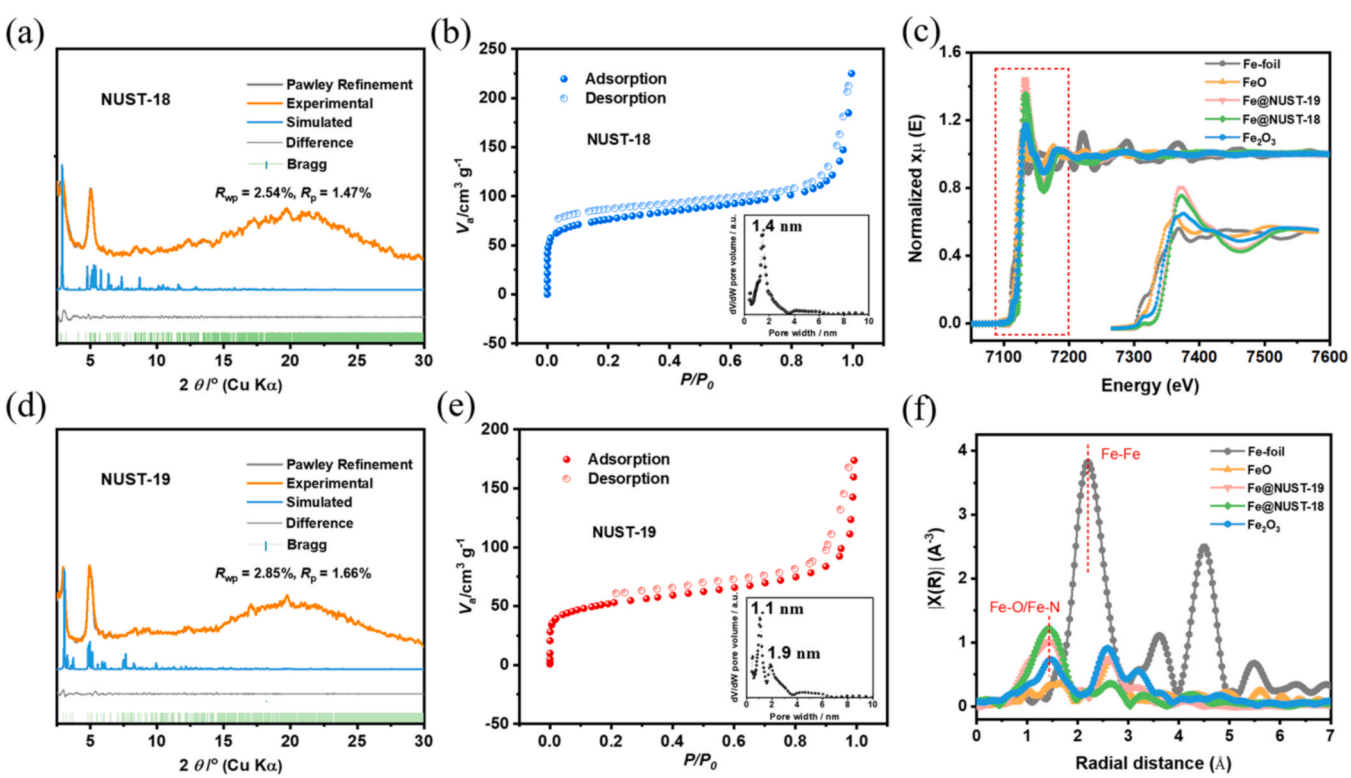

Fig. 2. (a, d) Experimental and theoretical XRD patterns of NUST-18/19. (b, e) N_2 adsorption-desorption isotherms for NUST-18/19 at 77 K (Inset: pore-size distribution for NUST-18/19). (c) Fe K-edge XANES spectra of Fe foil, FeO, Fe_2O_3, and Fe@ NUST-18/19. (f) Fourier transforms of Fe K-edge EXAFS spectra of Fe foil, FeO, Fe_2O_3, and Fe@ NUST-18/19.

by N_2 adsorption and desorption analysis at 77 K. Both adsorption curves exhibited a sharp increase at low pressure with the type-I isotherm, revealing their microporous structure. The application of the Brunauer-Emmett-Teller (BET) model resulted in the surface areas of 276 $m^2 g^{-1}$ for NUST-18 (Fig. 2b) and 188 $m^2 g^{-1}$ for NUST-19 (Fig. 2e). The pore size distributions were provided by nonlocal density functional theory (NLDFT), the result showed the narrow distribution centered at 1.4 nm for NUST-18, 1.1 nm/1.9 nm for NUST-19, which was in accordance with the pore sizes anticipated from its crystal structure (Fig. S9).

3.2. NRR test

For a long time, noble metal catalysts (*e.g.* Au, Pd, Ru, Rh) have long been considered as effective catalysts to achieve NRR. However, low abundance and high cost hinder the future large-scale application of precious metal catalysts. In nature, nitrogen-fixing bacteria can use more abundant transition metals around, such as molybdenum, iron and vanadium, as catalytic active centers for N_2 fixation. Based on this, the transition metal iron and copper ions were coordinated to the center of the porphyrin unit by post modification. The NUST-18/19 were added to a mixture of DMF and methanol (v/v, 3/1) containing copper acetate or iron acetate, stirred at room temperature for 24 h, and filtered to obtain Cu@NUST-18/19, Fe@NUST-18/19. PXRD shows that after metal ion modification, the COFs still retains a certain crystalline state (Fig. S20, S21). The successful coordination of metal ions was further confirmed by X-ray photoelectron spectroscopy (XPS). The survey XPS spectrum identifies the co-existence of Cu, Fe, C, and N elements. In the fitted high-resolution N 1s XPS spectrum, the Cu-N and Fe-N coordination peak were observed at 398.2 eV and 398.5 eV with the obvious displacement of the peak compared to the pristine COFs, which indicates the successful coordination of metal ions (Fig. S26-S29) [46].

In addition, XAS measurements were used to analyze the oxidation state and coordination environment of Fe in the two COFs. The Fe K-side X-ray absorption near-side structure (XANES) spectra (Fig. 2c), the Fe@NUST-18/19 show that the main absorption peak at 7133.1 eV is similar to Fe_2O_3 (7133.9 eV), but different from FeO (7130.2 eV). It can be concluded that the oxidation valence of Fe atom in the material is + 3. This indicates that Fe^{2+} (present in ferrous acetate as a precursor to the synthetic material) was oxidized to Fe^{3+} during insertion process [47]. The difference between the Fe@NUST-18/19 and the pre-edge peaks of the Fe foil excluded the presence of metallic Fe. The local structures of the Fe@NUST-18/19 were analyzed by extended X-ray absorption fine structure characterization (EXAFS). The Fe-N coordination characteristic signal appears at 1.44 Å (Fig. 2f), while the Fe-Fe bonding characteristic signal is missing at 2.20 Å, which verifies the retained Fe-N coordination in the sample [48].

The electrochemical NRR activity of as-formed catalysts were evaluated in a flow-type electrolytic cell with a Nafion-115 separation membrane in 0.1 M Na_2SO_4 aqueous electrolyte, wherein the catalysts onto a carbon paper substrate (mass loading: 0.20 mg cm^{-2}) were employed as the working electrode. All tests follow the rigorous experimental protocols to obtain reliable proof of NRR performances, and all tests did not require *iR*-compensation [49,50]. Firstly, linear sweep voltammetries (LSVs) were tested in N_2- or Ar-saturated 0.1 M Na_2SO_4 electrolytes (Fig. 3a), where the polarization curve in N_2-saturated electrolyte is lower than that of Ar-counterpart in all tested intervals indicating that N_2 is activated on the catalyst surface and inhibits H adsorption, so N_2 may participate in the electron-gaining reaction at the cathode.

Subsequently, chronoamperometric tests (I-T) were operated from − 0.4 to − 0.8 V (*vs.* RHE) to quantify NH_3 and other possible byproducts *via* the indophenol blue and Watt-Chrisp methods, respectively (Fig. 3b and Fig. S32-S35) [51,52]. The UV-vis spectra of the corresponding potential solution have obvious absorption at 655 nm, confirming that NH_3 is generated from NRR (Fig. S36). Strikingly, the maximum NH_3 yield rate and Faradaic efficiency of Fe@NUST-18 are 94.26 ± 4.9 μg h^{-1} mg^{-1} and 18.37 ± 0.96 % at − 0.5 V (*vs.* RHE,

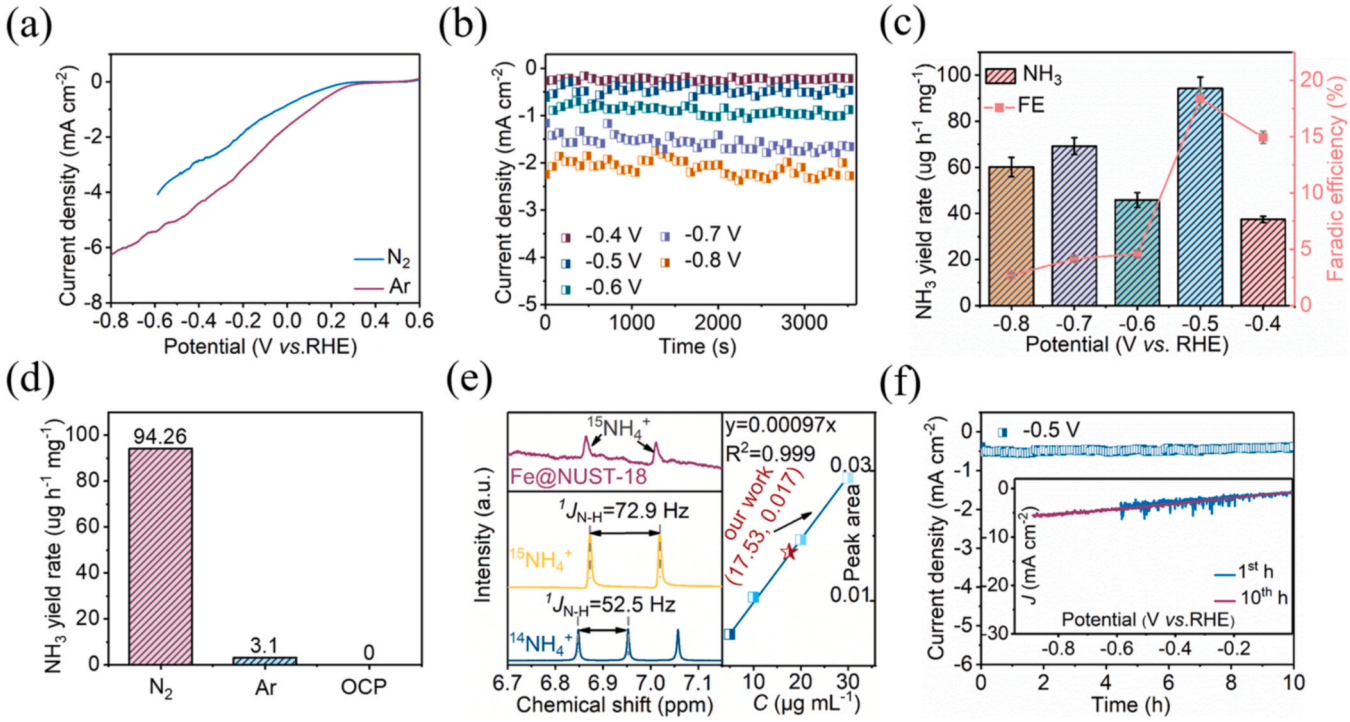

Fig. 3. Electrochemical NRR performances of Fe@NUST-18. (a) LSV curves recorded with a scan rate of 5 mV s^{-1} in N_2-saturated and Ar-saturated electrolytes. (b) Chronoamperometry curves in N_2-saturated electrolyte. (c) NH_3 yield rates and Faradaic efficiencies (FEs) at different applied potentials. (d) NH_3 yield rates at different conditions for 1 hr. (e) 500 MHz ^1H NMR spectra and calibration curve of NRR products tested at − 0.5 V (*vs.* RHE) for 4 hrs using $^{15}N_2$ feeding source. (f) Chronoamperometric test for 10 hrs at − 0.5 V (*vs.* RHE, inset: LSV plots before and after chronoamperometric tests).

Fig. 3c) and no any N_2H_4 byproducts was detected during the reaction process, which indicates that Fe@NUST-18 has excellent NRR activity and selectivity to NH_3 (Fig. S37). Next, several control experiments were performed to determine that the NH_3 produced by NRR came from N_2 (Fig. 3d and S38). When electrolysing Fe@NUST-18 at open circuit potential (OCP, in 0.1 M N_2-saturated Na_2SO_4 electrolyte) no NH_3 was produced, indicating that no cathodic reaction can be driven at OCP. Also, almost no NH_3 was detected of Fe@NUST-18 in 0.1 M Ar-saturated Na_2SO_4 electrolyte at − 0.5 V (*vs.* RHE), combined with its large current density, suggests that only HER side reactions can occur in the absence of N_2 (Fig. S38). In addition, ^{15}N isotope labelling experiments were conducted at − 0.5 V (*vs.* RHE) for accurate quantification of the NH_3 product from Fe@NUST-18. As shown in Fig. 3e, the ^{1}H nuclear magnetic resonance (NMR) spectra show a doublet signal closely matched to standard signals of $^{15}NH_4^+$ instead of triplet signal when using $^{15}N_2$ as the gas supply; therefore the feed gas was again confirmed to be the only nitrogen source. The corresponding NH_3 yield rate was 87.65 μg h^{-1} mg^{-1} (17.53 μg h^{-1} cm^{-2}), which is consistent with the results obained from other methods, demonstrating the reliability of the experimental results (Fig. 3e, S39). Further, Fe@NUST-18 showed excellent stability during the electrochemical cycling tests at − 0.5 V (*vs.* RHE). The strong stability can also be proved by negligible alternations of LSV, structure and morphology for Fe@NUST-18 after durability test (Fig. 3f, S40, S41). For the definite decrease in ammonia yield rate and FE at − 0.6 V, maybe due to i) Competing HER: One of the primary challenges in electrocatalytic NRR for ammonia production at negative potentials is the competition with the HER. At − 0.6 V, the HER may become more kinetically favorable, leading to a significant consumption of electrons that would have otherwise been used for the NRR. This competition can result in a decreased NH_3 yield rate and FE for ammonia production. ii) Changes in active site behavior: The behavior of catalytic active sites can vary depending on the applied potential. At − 0.6 V, there may be a change in the adsorption strength of N_2 or intermediates on the catalyst surface. This change can affect the progression of the reaction towards NH_3 formation. iii) Electrolyte interactions: The applied potential can influence how the electrolyte interacts with the catalyst surface. At − 0.6 V, there might be increased interactions between the electrolyte ions and the catalyst, which could block some active sites, thereby decreasing ammonia yield. However, as the potential is further increased, this blockage may decrease, resulting in the observed results presented in the manuscript. iv) Mass transport limitations: More negative potentials can lead to higher current densities and increased gas bubble formation. This can cause mass transport issues, reducing the availability of N_2 at the electrode surface, which in turn affects the ammonia yield rate. Considering these potential reasons, the observed decrease in ammonia yield rate at − 0.6 V emphasizes the multifaceted nature of electrocatalytic ammonia synthesis. It requires a delicate balance between optimizing the conditions for NRR, minimizing competing reactions, and ensuring the stability and availability of active sites.

To elucidate the advantages of the Fe@NUST-18, we compared the NRR activities of Fe@NUST-18, Cu@NUST-18 and NUST-18. It is shown that the current density of Fe@NUST-18 (Q = 1.75 C) is much larger than that of Cu@NUST-18 (Q = 1.24 C) and NUST-18 (Q = 0.42 C) at − 0.5 V (Fig. 4a). In addition, the NH_3 yield and FE of Fe@NUST-18 are 94.26 ± 4.9 μg h^{-1} mg^{-1} and 18.37 ± 0.96 % at − 0.5 V (*vs.* RHE), which outperform Cu@NUST-18 (20.94 ± 0.86 μg h^{-1} mg^{-1} and 5.72 ± 0.23 %) and NUST-18 (4.12 ± 0.27 μg h^{-1} mg^{-1} and 3.55 ± 0.28 %), which suggests that metals, especially Fe, act as active sites for NRR to drive the entire process (Fig. 4b). Further, to understand the intrinsic activity of Fe@NUST-18, the NH_3 yield rates have been normalized according to electrochemically specific areas (ECSA, Fig. S42). As shown in Fig. 4c, the normalized NH_3 yield rate of Fe@NUST-18 (3.73 mg h^{-1} m^{-2}) and Cu@NUST-18 (2.63 mg h^{-1} m^{-2}) are 5.57 and 3.91 times higher than NUST-18 derivatives (0.67 mg h^{-1} m^{-2}). Finally, we have performed similar steps to test the performance of Fe@NUST-19 and comparative samples. Similarly, Fe@NUST-19 has similar LSV, I-T and UV curve characteristics to Fe@NUST-18 (Fig. S43-S47). Also, the maximum NH_3

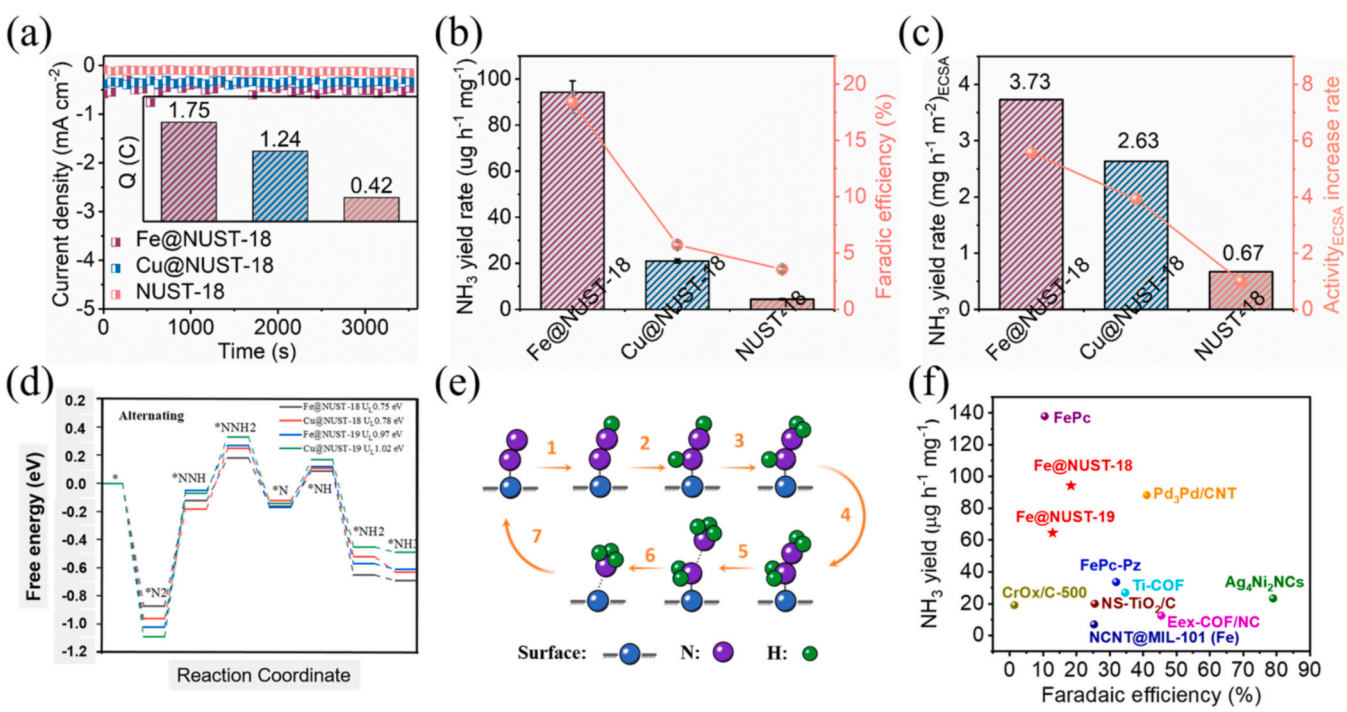

Fig. 4. (a) Chronoamperometry curves of Fe@NUST-18, Cu@NUST-18 and NUST-18 in N_2-saturated 0.1 M Na_2SO_4 solution at − 0.5 V (*vs.* RHE); the inset of (a) shows the comparison of the total charge consumed after 1 hr of testing. (b) NH_3 yield rates and Faradaic efficiencies (FEs) of Fe@NUST-18, Cu@NUST-18 and NUST-18. (c) NH_3 yield rates normalized according to ECSA for NRR. (d) The NRR Gibbs free energy diagram of Fe@NUST-18/19, Cu@NUST-18/19 through alternating pathway. (e) NRR reaction pathway diagram through alternating pathway. (e) Schematic diagram of NRR reaction mechanism. (f) Comparison of the NRR performance for the state-of-the-art NRR electrocatalysts under similar test conditions.

yield of Fe@NUST-19 is 64.49 ± 3.12 μg h^{-1} mg^{-1} at − 0.6 V (*vs.* RHE, Fig. S43), which outperform other counterparts such as Cu@NUST-19 (17.55 ± 0.50 μg h^{-1} mg^{-1}) and NUST-19 (4.02 ± 0.16 μg h^{-1} mg^{-1}, Fig. S45). In addition, the maximum FE of Fe@NUST-19 is 12.85 ± 0.62 %, which is similar to Cu@NUST-19 (15.18 ± 0.44 %) and far superior to NUST-19 (3.22 ± 0.13 %). Next, a series of control experiments to identify that the NH_3 produced from NRR is sourced from N_2 rather than from external pollutions (Fig. S46). The Fe@NUST-19 also exhibit excellent stability in 0.1 M Na_2SO_4 for operating after 10 hrs under − 0.6 V (*vs.* RHE, Fig. S46). To our best knowledge, the Fe@NUST-18/19 are among the most excellent inorganic hybrid or 2D COFs NRR electrocatalysts reported thus far (Fig. 4f, Table S2). Therefore, the Fe@ 3D COFs can afford intrinsic activites for NRR originated from its excellent electronic structure and 3D structural advantages, which can be demonstrated by comparison with the corresponding amorphous electrode (Fig. S56-S57). The mechanism of NRR reaction was explained by theoretical calculation (detail in the ESI). The Gibbs free energy diagrams for the NRR on metallized COFs along the distal, alternating (Fig. 4d), enzymatic and Mix mechanisms were shown in Fig. S69. The results show that the enzymatic mechanism was the best one among the known four NRR mechanisms and Fe@NUST-18 shown lowest the energy barrier in the PDS process of first hydrogenation of N_2 (Fig. 4e).

4. Conclusions

In conclusion, two 3D COFs based on 8-connected porphyrin unit with novel ***scu*** and ***flu*** topologies were constructed *via* reticular chemistry. Thanks to the unique structural advantages of the 3D COF, as well as the good planar N_4 coordination site of the porphyrin group and the large π-conjugated system, two 3D COFs with more exposed Fe-N_4 active sites present highly efficient electrocatalytic reduction of nitrogen to ammonia with excellent NH_3 yield and Faradaic efficiency (94.26 ± 4.9 μg h^{-1} mg^{-1} and 18.37 ± 0.96 % at −0.5 V *vs* RHE), among the highest values of most inorganic hybrid and organic materials.This work not only enriches the topology of 3D COFs, but also provides the basis for the development of 3D por-COF NRR electrocatalysts with M-N_4 active sites, thus providing ideas for the rational design of high-performance NRR electrocatalysts.

CRediT authorship contribution statement

Zhen Shan: Methodology, Investigation, Data analysis, Crystal Structural Analysis, Theoretical Calculation. **Yuntong Sun:** Methodology, Data analysis, Structure Simulation, Theoretical Calculation. **Miaomiao Wu:** Theoretical Calculation. **Yingtang Zhou:** Electrocatalytic Nitrogen Reduction. **Jinjian Wang:** Theoretical Calculation. **Sheng Chen:** Funding acquisition. **Rui Wang:** Funding acquisition. **Gen Zhang:** Conceptualization, Writing with the input from the other authors, Funding acquisition, Project administration, Supervision.

Declaration of Competing Interest

The authors declare that they have no known competing financial interests or personal relationships that could have appeared to influence the work reported in this paper.

Data Availability

Data will be made available on request.

Acknowledgements

This work was financially supported by the Medical Innovation and Development Project of Lanzhou University (lzuyxcx-2022-156), CAMS Innovation Fund for Medical Sciences (CIFMS, 2019-I2M-5-074, 2021-I2M-1-026, 2021-I2M-3-001, 2022-I2M-2-002), the National Natural Science Foundation of China (22171136, 92163124), the Natural Science Foundation of Jiangsu Province (BK20220079), the Fundamental Research Funds for the Central Universities (30921011102, 30921013103), and the Startup Funding from Nanjing University of Science and Technology. G.Z. acknowledges the support of the Thousand Young Talent Plan.

Appendix A. Supporting information

Supplementary data associated with this article can be found in the online version at doi:10.1016/j.apcatb.2023.123418.

References

[1] D.E. McCoy, T. Feo, T.A. Harvey, R.O. Prum, Structural absorption by barbule microstructures of super black bird of paradise feathers, Nat. Commun. 9 (1) (2018), https://doi.org/10.1038/s41467-017-02088-w.
[2] J.G. Chen, R.M. Crooks, L.C. Seefeldt, K.L. Bren, R.M. Bullock, M.Y. Darensbourg, et al., Beyond fossil fuel-driven nitrogen transformations, Science 360 (2018), eaar6611, https://doi.org/10.1126/science.aar6611.
[3] M. Kunitski, N. Eicke, P. Huber, J. Köhler, S. Zeller, J. Voigtsberger, et al., Double-slit photoelectron interference in strong-field ionization of the neon dimer, Nat. Commun. 10 (1) (2019), https://doi.org/10.1038/s41467-018-07882-8.
[4] G. Qing, R. Ghazfar, S.T. Jackowski, F. Habibzadeh, M.M. Ashtiani, C.-P. Chen, et al., Recent advances and challenges of electrocatalytic N_2 reduction to ammonia, Chem. Rev. 120 (2020) 5437–5516, https://doi.org/10.1021/acs.chemrev.9b00659.
[5] S. Liu, Y. Liu, Z. Cheng, Y. Tan, Y. Ren, T. Yuan, et al., Catalytic role of adsorption of electrolyte/molecules as functional ligands on two-dimensional TM-N_4 monolayer catalysts for the electrocatalytic nitrogen reduction reaction, ACS Appl. Mater. Interfaces 13 (2021) 40590–40601, https://doi.org/10.1021/acsami.1c10367.
[6] X. Liang, H. Zhu, X. Yang, S. Xue, Z. Liang, X. Ren, et al., Recent advances in designing efficient electrocatalysts for electrochemical nitrate reduction to ammonia, Small Struct. (2022), 2200202, https://doi.org/10.1002/sstr.202200202.
[7] R. Li, K. Xiang, Z. Liu, Z. Peng, Y. Zou, S. Wang, Recent advances in upgrading of low-cost oxidants to value-added products by electrocatalytic reduction reaction, Adv. Funct. Mater. 32 (2022), 2208212, https://doi.org/10.1002/adfm.202208212.
[8] S. Paul, S. Sarkar, A. Adalder, S. Kapse, R. Thapa, U.K. Ghorai, Strengthening the metal center of Co-N4 active sites in a 1D-2D heterostructure for nitrate and nitrogen reduction reaction to ammonia, ACS Sustain Chem. Eng. 11 (2023) 6191–6200, https://doi.org/10.1021/acssuschemeng.2c07114.
[9] T. Wu, M.M. Melander, K. Honkala, Coadsorption of nrr and her intermediates determines the performance of Ru-N_4 toward electrocatalytic N_2 reduction, ACS Catal. 12 (2022) 2505–2512, https://doi.org/10.1021/acscatal.1c05820.
[10] S. Chen, H. Jang, J. Wang, Q. Qin, X. Liu, J. Cho, Bimetallic metal-organic framework-derived MoFe-Pc microspheres for electrocatalytic ammonia synthesis under ambient conditions, J. Mater. Chem. A 8 (2020) 2099–2104, https://doi.org/10.1039/C9TA10524G.
[11] H. Zhong, M. Wang, M. Ghorbani-Asl, J. Zhang, K.H. Ly, Z. Liao, et al., Boosting the electrocatalytic conversion of nitrogen to ammonia on metal-phthalocyanine-based two-dimensional conjugated covalent organic frameworks, J. Am. Chem. Soc. 143 (2021) 19992–20000, https://doi.org/10.1021/jacs.1c11158.
[12] U.K. Ghorai, S. Paul, B. Ghorai, A. Adalder, S. Kapse, R. Thapa, et al., Scalable production of cobalt phthalocyanine nanotubes: efficient and robust hollow electrocatalyst for ammonia synthesis at room temperature, ACS Nano 15 (2021) 5230–5239, https://doi.org/10.1021/acsnano.0c10596.
[13] S. Xu, Y. Ding, J. Du, Y. Zhu, G. Liu, Z. Wen, et al., Immobilization of iron phthalocyanine on pyridine-functionalized carbon nanotubes for efficient nitrogen reduction reaction, ACS Catal. 12 (2022) 5502–5509, https://doi.org/10.1021/acscatal.2c00188.
[14] A.P. Côté, A.I. Benin, N.W. Ockwig, M. O'Keeffe, A.J. Matzger, O.M. Yaghi, Porous, crystalline, covalent organic frameworks, Science 310 (2005) 1166–1170, https://doi.org/10.1126/science.1120411.
[15] F. Haase, B.V. Lotsch, Solving the cof trilemma: towards crystalline, stable and functional covalent organic frameworks, Chem. Soc. Rev. 49 (2020) 8469–8500, https://doi.org/10.1039/D0CS01027H.
[16] S.T. Emmerling, R. Schuldt, S. Bette, L. Yao, R.E. Dinnebier, J. Kästner, et al., Interlayer interactions as design tool for large-pore COFs, J. Am. Chem. Soc. 143 (2021) 15711–15722, https://doi.org/10.1021/jacs.1c06518.
[17] X. Zhao, P. Pachfule, A. Thomas, Covalent organic frameworks (COFs) for electrochemical applications, Chem. Soc. Rev. 50 (2021) 6871–6913, https://doi.org/10.1039/D0CS01569E.
[18] G.-B. Wang, K.-H. Xie, H.-P. Xu, Y.-J. Wang, F. Zhao, Y. Geng, et al., Covalent organic frameworks and their composites as multifunctional photocatalysts for efficient visible-light induced organic transformations, Coord. Chem. Rev. 472 (2022), 214774, https://doi.org/10.1016/j.ccr.2022.214774.
[19] Y.-N. Gong, W. Zhong, Y. Li, Y. Qiu, L. Zheng, J. Jiang, et al., Regulating photocatalysis by spin-state manipulation of cobalt in covalent organic

frameworks, J. Am. Chem. Soc. 142 (2020) 16723–16731, https://doi.org/10.1021/jacs.0c07206.
[20] M. Chen, H. Li, C. Liu, J. Liu, Y. Feng, A.G.H. Wee, et al., Porphyrin- and porphyrinoid-based covalent organic frameworks (COFs): from design, synthesis to applications, Coord. Chem. Rev. 435 (2021), 213778, https://doi.org/10.1016/j.ccr.2021.213778.
[21] S. Liu, T. Qian, M. Wang, H. Ji, X. Shen, C. Wang, et al., Proton-filtering covalent organic frameworks with superior nitrogen penetration flux promote ambient ammonia synthesis, Nat. Catal. 4 (2021) 322–331, https://doi.org/10.1038/s41929-021-00599-w.
[22] S. Huang, K. Chen, T.-T. Li, Porphyrin and phthalocyanine based covalent organic frameworks for electrocatalysis, Coord. Chem. Rev. 464 (2022), 214563, https://doi.org/10.1016/j.ccr.2022.214563.
[23] X. Shen, S. Liu, X. Xia, M. Wang, H. Ji, Z. Wang, et al., Interfacial microextraction boosting nitrogen feed for efficient ambient ammonia synthesis in aqueous electrolyte, Adv. Funct. Mater. 32 (2022), 2109422, https://doi.org/10.1002/adfm.202109422.
[24] C.-Y. Lin, L. Zhang, Z. Zhao, Z. Xia, Design principles for covalent organic frameworks as efficient electrocatalysts in clean energy conversion and green oxidizer production, Adv. Mater. 29 (2017), 1606635, https://doi.org/10.1002/adma.201606635.
[25] M. Wang, S. Liu, T. Qian, J. Liu, J. Zhou, H. Ji, et al., Over 56.55 % faradaic efficiency of ambient ammonia synthesis enabled by positively shifting the reaction potential, Nat. Commun. 10 (2019), 341, https://doi.org/10.1038/s41467-018-08120-x.
[26] J.-Y. Yue, Y.-T. Wang, X. Wu, P. Yang, Y. Ma, X.-H. Liu, et al., Two-dimensional porphyrin covalent organic frameworks with tunable catalytic active sites for the oxygen reduction reaction, Chem. Commun. 57 (2021) 12619–12622, https://doi.org/10.1039/D1CC04928C.
[27] M. Wang, S. Liu, H. Ji, T. Yang, T. Qian, C. Yan, Salting-out effect promoting highly efficient ambient ammonia synthesis, Nat. Commun. 12 (2021) 3198, https://doi.org/10.1038/s41467-021-23360-0.
[28] S. Lin, C.S. Diercks, Y.-B. Zhang, N. Kornienko, E.M. Nichols, Y. Zhao, et al., Covalent organic frameworks comprising cobalt porphyrins for catalytic CO_2 reduction in water, Science 349 (2015) 1208–1213, https://doi.org/10.1126/science.aac8343.
[29] Q. Wu, R.-K. Xie, M.-J. Mao, G.-L. Chai, J.-D. Yi, S.-S. Zhao, et al., Integration of strong electron transporter tetrathiafulvalene into metalloporphyrin-based covalent organic framework for highly efficient electroreduction of CO_2, ACS Energy Lett. 5 (2020) 1005–1012, https://doi.org/10.1021/acsenergylett.9b02756.
[30] R. Chen, J.-L. Shi, Y. Ma, G. Lin, X. Lang, C. Wang, Designed synthesis of a 2D porphyrin-based sp2 carbon-conjugated covalent organic framework for heterogeneous photocatalysis, Angew. Chem. Int. Ed. 58 (2019) 6430–6434, https://doi.org/10.1002/anie.201902543.
[31] Y. Qian, D. Li, Y. Han, H.-L. Jiang, Photocatalytic molecular oxygen activation by regulating excitonic effects in covalent organic frameworks, J. Am. Chem. Soc. 142 (2020) 20763–20771, https://doi.org/10.1021/jacs.0c09727.
[32] S.-Y. Chi, Q. Chen, S.-S. Zhao, D.-H. Si, Q.-J. Wu, Y.-B. Huang, et al., Three-dimensional porphyrinic covalent organic frameworks for highly efficient electroreduction of carbon dioxide, J. Mater. Chem. A 10 (2022) 4653–4659, https://doi.org/10.1039/D1TA10991J.
[33] Q. Zhu, X. Wang, R. Clowes, P. Cui, L. Chen, M.A. Little, et al., 3d cage cofs: a dynamic three-dimensional covalent organic framework with high-connectivity organic cage nodes, J. Am. Chem. Soc. 142 (2020) 16842–16848, https://doi.org/10.1021/jacs.0c07732.
[34] H. Li, J. Ding, X. Guan, F. Chen, C. Li, L. Zhu, et al., Three-dimensional large-pore covalent organic framework with stp topology, J. Am. Chem. Soc. 142 (2020) 13334–13338, https://doi.org/10.1021/jacs.0c06485.
[35] Y. Wang, C. Wu, W. Sun, Q. Pan, W. Hao, H. Liu, et al., Triptycene-based three-dimensional covalent organic frameworks with stp topology of honeycomb structure, Mater. Chem. Front. 5 (2021) 944–949, https://doi.org/10.1039/D0QM00846J.
[36] Z. Li, L. Sheng, H. Wang, X. Wang, M. Li, Y. Xu, et al., Three-dimensional covalent organic framework with ceq topology, J. Am. Chem. Soc. 143 (2021) 92–96, https://doi.org/10.1021/jacs.0c11313.
[37] Z. Li, L. Sheng, C. Hsueh, X. Wang, H. Cui, H. Gao, et al., Three-dimensional covalent organic frameworks with hea topology, Chem. Mater. 33 (2021) 9618–9623, https://doi.org/10.1021/acs.chemmater.1c03156.
[38] C. Yu, H. Li, Y. Wang, J. Suo, X. Guan, R. Wang, et al., Three-dimensional triptycene-functionalized covalent organic frameworks with hea net for hydrogen adsorption, Angew. Chem. Int. Ed. 61 (2022), e202117101, https://doi.org/10.1002/anie.202117101.
[39] C. Gropp, T. Ma, N. Hanikel, O.M. Yaghi, Design of higher valency in covalent organic frameworks, Science 370 (2020), eabd6406, https://doi.org/10.1126/science.abd6406.
[40] Z. Shan, M. Wu, D. Zhu, X. Wu, K. Zhang, R. Verduzco, et al., 3D covalent organic frameworks with interpenetrated pcb topology based on 8-connected cubic nodes, J. Am. Chem. Soc. 144 (2022) 5728–5733, https://doi.org/10.1021/jacs.2c01037.
[41] X. Xu, P. Cai, H. Chen, H.-C. Zhou, N. Huang, Three-dimensional covalent organic frameworks with she topology, J. Am. Chem. Soc. 144 (2022) 18511–18517, https://doi.org/10.1021/jacs.2c07733.
[42] W. Liu, L. Gong, Z. Liu, Y. Jin, H. Pan, X. Yang, et al., Conjugated three-dimensional high-connected covalent organic frameworks for lithium-sulfur batteries, J. Am. Chem. Soc. 144 (2022) 17209–17218, https://doi.org/10.1021/jacs.2c07596.
[43] L. Liao, X. Guan, H. Zheng, Z. Zhang, Y. Liu, H. Li, et al., Three-dimensional microporous and mesoporous covalent organic frameworks based on cubic building units, Chem. Sci. 13 (2022) 9305–9309, https://doi.org/10.1039/D2SC02365B.
[44] C. Gong, H. Wang, G. Sheng, X. Wang, X. Xu, J. Wang, et al., Synthesis and visualization of entangled 3D covalent organic frameworks with high-valency stereoscopic molecular nodes for gas separation, Angew. Chem. Int. Ed. 61 (2022), e202204899, https://doi.org/10.1002/anie.202204899.
[45] F. Jin, E. Lin, T. Wang, S. Geng, T. Wang, W. Liu, et al., Bottom-up synthesis of 8-connected three-dimensional covalent organic frameworks for highly efficient ethylene/ethane separation, J. Am. Chem. Soc. 144 (2022) 5643–5652, https://doi.org/10.1021/jacs.2c01058.
[46] J. Guo, C.-Y. Lin, Z. Xia, Z. Xiang, A pyrolysis-free covalent organic polymer for oxygen reduction, Angew. Chem. Int. Ed. 57 (2018) 12567–12572, https://doi.org/10.1002/anie.201808226.
[47] S. Shang, W. Xiong, C. Yang, B. Johannessen, R. Liu, H.-Y. Hsu, et al., Atomically dispersed iron metal site in a porphyrin-based metal-organic framework for photocatalytic nitrogen fixation, ACS Nano 15 (2021) 9670–9678, https://doi.org/10.1021/acsnano.0c10947.
[48] M. Qiao, Y. Wang, Q. Wang, G. Hu, X. Mamat, S. Zhang, et al., Hierarchically ordered porous carbon with atomically dispersed FeN_4 for ultraefficient oxygen reduction reaction in proton-exchange membrane fuel cells, Angew. Chem. Int. Ed. 59 (2020) 2688–2694, https://doi.org/10.1002/anie.201914123.
[49] S.Z. Andersen, V. Colic, S. Yang, J.A. Schwalbe, A.C. Nielander, J.M. McEnaney, et al., A rigorous electrochemical ammonia synthesis protocol with quantitative isotope measurements, Nature 570 (2019) 504–508, https://doi.org/10.1038/s41586-019-1260-x.
[50] F. Hanifpour, A. Sveinbjornson, C.P. Canales, E. Skulason, H.D. Flosadottir, Preparation of nafion(r) membranes for reliable ammonia quantification in nitrogen reduction reaction experiments, Angew. Chem. Int. Ed. 59 (2020) 22938–22942, https://doi.org/10.1002/anie.202007998.
[51] Y. Sun, L. Yu, S. Xu, S. Xie, L. Jiang, J. Duan, et al., Battery-driven N_2 electrolysis enabled by high-entropy catalysts: from theoretical prediction to prototype model, Small 18 (2022), e2106358, https://doi.org/10.1002/smll.202106358.
[52] Y. Sun, S. Ding, B. Xia, J. Duan, M. Antonietti, S. Chen, Biomimetic FeMo(Se, Te) as joint electron pool promoting nitrogen electrofixation, Angew. Chem. Int Ed. 61 (2022), e202115198, https://doi.org/10.1002/anie.202115198.